ChemComm

COMMUNICATION

View Article Online
View Journal

Cite this: DOI: 10.1039/d6cc01200k

Received 26th February 2026,
Accepted 21st April 2026

DOI: 10.1039/d6cc01200k

rsc.li/chemcomm

Cobalt polyoxometalate–LDH hybrids: pH-switchable molecular catalysts to confined cobalt oxide oxygen evolution layers

Javier Quirós-Huerta, Ramón Torres-Cavanillas, Susana Ochando-Pariente, Eugenio Coronado and Joaquín Soriano-López *

Intercalating Co-POMs into the LDH lamellar space effectively boosts their OER activity at neutral pH. In alkaline media, Co-POMs decompose into tunable layered cobalt oxide species within the LDH gallery, controlled by Co-POM nuclearity. The latter is a novel method for preparing layered oxides using the LDH galleries as nanoreactors.

The rise in global energy demands and the broader goals of carbon neutrality urge us to rapidly change our energy production paradigm toward cleaner alternatives.[1] Green hydrogen production *via* water electrolysis is an affordable method for storing renewable energy, aiming to replace fossil fuel usage and mitigate anthropogenic effects on climate change.[2,3] In the water electrolysis process, the water oxidation half-reaction, also known as the oxygen evolution reaction (OER), is a bottleneck preventing efficient, large-scale hydrogen production.[4] The reason is that the OER is associated with high thermodynamic and kinetic barriers imposed by a complex four-electron transfer coupled with proton migration, O–H bond cleavage, and O–O bond formation, often requiring the use of scarce, geographically concentrated noble metal-based catalysts.[5–7] Consequently, the design and optimisation of high-performance OER electrocatalysts based on Earth-abundant elements is a major research priority.[8,9]

Polyoxometalates (POMs) are nanosized molecular oxides attractive as OER catalysts due to their robustness under oxidizing conditions, their high amenability and molecular versatility, and their ability to undergo redox processes without altering their molecular structure.[10,11] Furthermore, they can be seen as molecular models of bulk oxides that aid the rationalisation and design of novel heterogeneous OER catalysts. Especially interesting are the cobalt-substituted polyoxometalates (Co-POMs), which have been intensively studied over the last 15 years as OER catalysts, showing excellent catalytic capabilities under a wide variety of pH conditions with outstanding stability under controlled conditions.[12–14] Moreover, structure–activity relationship studies advanced in the better understanding of their properties to fine-tune their OER capabilities.[15–19] As molecular, water-soluble clusters, they need to be processed to work under heterogeneous conditions.[20–22] In this respect, 2D materials can play a crucial role in the fabrication of heterogeneous, Co-POM-based OER catalysts displaying a high surface area, mechanical strength, and excellent chemical stability. Additionally, the ultrathin nature of 2D materials minimizes the electron migration pathways, promoting charge separation and reducing recombination.[23,24] For instance, we have recently shown that intercalating $[Co_4(H_2O)_2(PW_9O_{34})_2]^{10-}$ (Co_4) in an OER inactive Mg_2Al layered double hydroxide (LDH) enhances the OER activity of Co_4 at close-to-neutral pH. Interestingly, due to the low stability of the Keggin moiety under alkaline conditions, the Co-POM undergoes hydrolytic transformation into an OER-active layered, mixed-valence Co(II/III) oxide within the LDH interlayers.[25] The latter suggests that LDHs can act as confined nanoplatforms to produce layered heterostructures of alternating oxides/hydroxides.

Here, we investigate the electrocatalytic OER activity of two Co-POMs, $[Co_9(H_2O)_6(OH)_3(HPO_3)_2(PW_9O_{34})_3]^{16-}$ (Co_9) and $[Co_4(H_2O)_2(P_2W_{15}O_{56})_2]^{16-}$ (Co_4-WD), intercalated into Mg_2Al-LDH. By comparing the displayed OER activities with those of our previously reported Co_4/Mg_2Al nanocomposite, we assess the influence of Co-POM nuclearity (Co_4 *vs.* Co_9) and the polyoxotungstate framework type (Co_4-Keggin *vs.* Co_4-Wells–Dawson) on the OER activity.

The Co-POMs/Mg_2Al hybrid nanocomposites were fabricated through a cation exchange process. Co-POM intercalation was confirmed by analysing the PXRD patterns of the as-synthesized nanocomposites shown in Fig. 1(a). The basal reflections of the pristine Mg_2Al-LDH display the expected peaks for a hydrotalcite-like material. The first peak corresponds to the (003) interlayer reflection and depends on the size of the anion present in the lamellar space. This peak appears at $2\theta = 11.54^\circ$,

Institut de Ciència Molecular, Universitat de València, Catedrático José Beltrán 2, Paterna 46980, Spain. E-mail: joaquin.soriano@uv.es

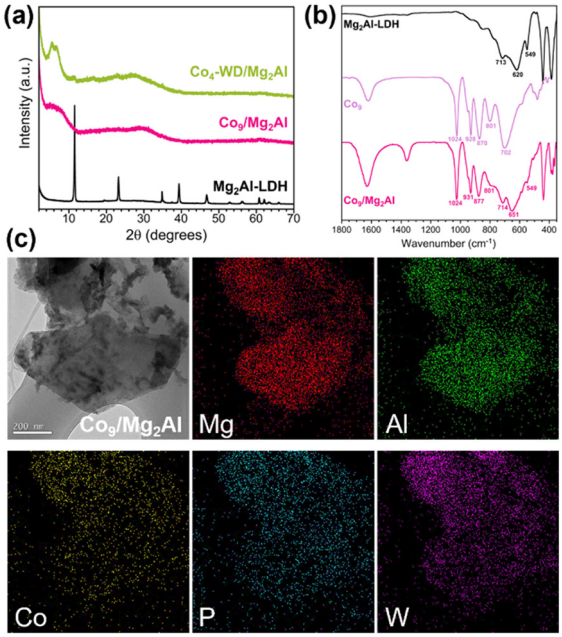

Fig. 1 (a) PXRD pattern of Mg_2Al-LDH compared to that of the freshly prepared nanocomposites. (b) FT-IR spectra of Mg_2Al-LDH, Co_9 POM, and Co_9/Mg_2Al. (c) TEM image and EDX mapping of Co_9/Mg_2Al.

corresponding to a basal spacing (d_{BS}) of 7.67 Å and an interlayer spacing of 2.87 Å, assuming an LDH layer thickness of 4.8 Å.[26] After Co-POM intercalation, the PXRD patterns become markedly broader and less defined, indicating a substantial loss of crystallinity and the onset of turbostratic disorder. This behaviour is consistent with the structural perturbation commonly observed when molecular species that can perturb the interlayer interaction are included in layered two-dimensional hosts.[27] Despite this reduced crystallinity, the broad reflection assigned to the (003) interlayer reflections of the Co-POM/LDH nanocomposites shifts to $2\theta = 5.2^\circ$ for Co_9/Mg_2Al and $2\theta = 4.9^\circ$ for Co_4-WD/Mg_2Al, with an estimated interlayer spacing of 12.19 Å and 13.23 Å, respectively. Therefore, considering that the length of the short axis of both POMs ranges between 1.0 and 1.5 nm, these interlayer space distances suggest that Co_9 is intercalated with the C_{3h} symmetrical axis perpendicular to the host layer of the LDH, whereas the C_{2h} symmetrical axis of Co_4-WD lies parallel to the host layer.

FT-IR spectra of the hybrid nanocomposites compared to those of the isolated materials demonstrate the appearance of electrostatic interactions and the formation of hydrogen bonds between the Co-POM framework and the LDH layers (Fig. 1(b) and Fig. S3). This is exemplified by a slight shift in the energies of the different vibration modes of the tungsten-oxide framework of the Co-POMs in the 700–950 cm^{-1} range and a shift in the O–M–O vibrations of the brucite-like layers of the LDH counterpart between 620 and 750 cm^{-1}. Moreover, the vibrations attributed to the P–O bond of the heteroatom displayed at 1026 cm^{-1} in Co_9 and at 1051 and 1082 cm^{-1} in Co_4-WD remain unaltered.

The compositional elements in the nanocomposites were analysed by ICP-MS, confirming the expected Mg:Al ratio of 2 : 1 after Co-POM intercalation (Table S1). Moreover, we estimated the LDH : Co-POM ratio for both nanocomposites to be $[Mg_{0.66}Al_{0.34}(OH)_2]:[(Co_9)_{0.029}]$ and $[Mg_{0.66}Al_{0.34}(OH)_2]:[(Co_4\text{-}WD)_{0.020}]$ for Co_9/Mg_2Al and Co_4-WD/Mg_2Al, respectively, which are similar values to our previously reported ratio of $[Mg_{0.64}Al_{0.36}(OH)_2]:[(Co_4)_{0.026}]$ for the Co_4/Mg_2Al nanocomposite.

TEM images of the nanocomposites show that the initial hexagonal crystals of Mg_2Al-LDH are partially broken during the chemical exfoliation step, whereas electron diffraction patterns show a pronounced turbostratic disorder due to an imperfect alignment in the restacking of the slabs from the swollen phase during Co-POM intercalation (Fig. 1(c) and Fig. S4, S5). Additionally, EDX mapping confirms the presence of all the expected elements and shows that the Co-POMs are homogeneously dispersed in the lamellar space of the LDH.

Fig. 2 presents the XPS spectra of the freshly prepared Co_9/Mg_2Al and Co_4-WD/Mg_2Al hybrids alongside those of the corresponding bare POMs and the Mg_2Al-LDH reference. In both hybrids, the Co 2p and W 4f signals coincide with those of the isolated POMs (Fig. 2(a) and (b)), while the Mg and Al contributions from the LDH lattice are also detected (Fig. 2(c) and (d)). Importantly, the binding energies of Co and W remain unchanged, demonstrating that the Co_4-WD and Co_9 clusters are incorporated into the LDH interlayer space without alteration of their redox state. In contrast, the LDH component exhibits a clear modification. As previously observed,[25] an additional contribution appears in the Al 2p region of the

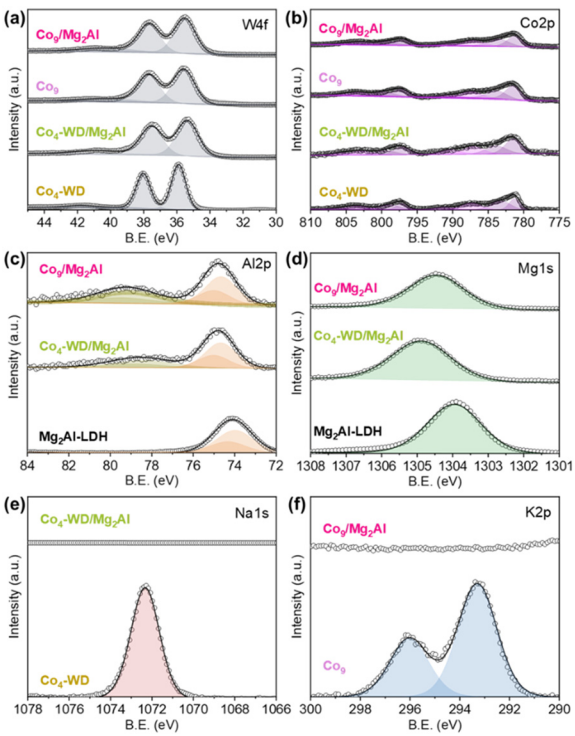

Fig. 2 XPS data of the as-synthesized Mg_2Al-LDH, Co_4-WD and Co_9 POMs, and Co_9/Mg_2Al and Co_4-WD/Mg_2Al nanocomposites. The high resolution XPS spectra correspond to (a) W 4f, (b) Co 2p, (c) Al 2p, (d) Mg 1s, (e) Na 1s, and (f) K 2p.

hybrids, indicating a change in the electronic environment of Al induced by the presence of the intercalated Co-POMs (Fig. 2(c)). This effect is consistent with a direct electrostatic interaction between the negatively charged Co-POM anions and the trivalent Al centres that carry the positive charge within the LDH layers. Further evidence of this interaction is provided by the Na 1s and K 2p regions (Fig. 2(e) and (f)). The characteristic counter-cations detected in the bare POMs (Na^+ for Co_4-WD and K^+ for Co_9) are absent in the corresponding hybrids. Their disappearance confirms that charge compensation is instead provided by the intrinsically cationic LDH framework, with the POMs residing in the lamellar space.

We then analysed the stability of the nanocomposites in the two electrolytes later employed in the OER measurements. The nanocomposites were immersed in the electrolytes under stirring for 72 hours. PXRD patterns (Fig. S6) and FT-IR spectra (Fig. S22) of the collected materials show that their structural integrity is maintained at pH 6.9. However, a clear structural change is observed at pH 14.2, in which the crystallinity of the LDH is recovered, accompanied by a decrease in the gallery spacing, and the main POM features in the FT-IR completely disappear. Moreover, EDX mapping confirms this behaviour, and as shown in Fig. S7 and S8, the Co-POMs are homogeneously dispersed in the LDH at pH 6.9, while W and P are barely detected at pH 14.2, with Co predominantly present in the LDH gallery as shown in Fig. S9 and S10. This result indicates that neither Keggin nor Wells–Dawson POM ligands are stable in alkaline media. In fact, it is well known that Keggin and Wells–Dawson POMs are only stable in acidic media,[28] while Co-POMs undergo hydrolytic decomposition in basic media.[29,30] Therefore, we can confirm that LDHs do not provide an appropriate environment for stabilising the intercalated POMs in alkaline media. In our case, Co-POM degradation results in the loss of W and P atoms from the nanocomposites, while Co is retained in the LDH gallery as a layered oxide/hydroxide formed *in situ* (*vide infra*).

The electrocatalytic OER activity of the hybrid nanocomposites was studied at neutral and alkaline pH. To allow for a fair comparison, the intrinsic activity of each hybrid was analysed by normalizing the current intensities displayed in the polarization curves by the roughness factor (R_F) of each electrode (Fig. 3(a), (b) and Fig. S11). We also compared the OER activity based on the Co content (Fig. S12) and confirmed O_2 evolution through RRDE experiments (Fig. S13). Despite offering the lowest ECSA value (Fig. 3(d)), Co_9/Mg_2Al outperforms the OER activity of both Co_4/Mg_2Al and Co_4-WD/Mg_2Al at neutral pH, agreeing with previous studies demonstrating the superior OER activity of Co_9.[31] Interestingly, the Co_4-WD/Mg_2Al hybrid displays comparable OER activity to Co_4/Mg_2Al. The Co_4-WD POM is commonly considered a poor OER catalyst,[12,32] whereby Keggin derivatives exhibit faster kinetics than Wells–Dawson derivatives, often associated with the higher steric hindrance imposed by larger POM ligands.[32] Our results suggest that the homogeneous dispersion of POMs in the interlayer space of the LDH, together with the confinement effects, results in a positive impact on the overall activity of the POMs. Under these

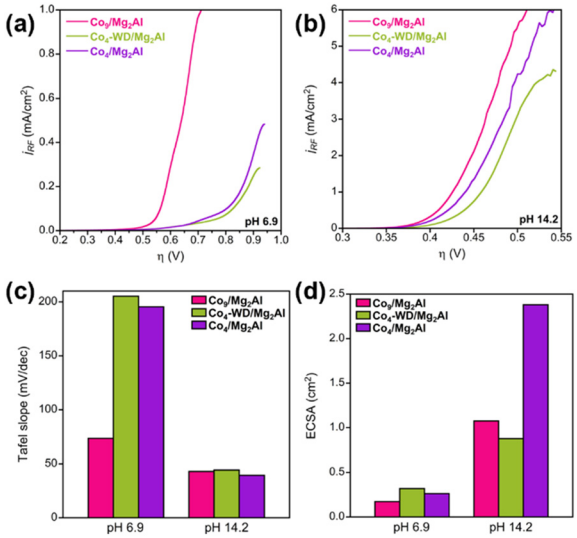

Fig. 3 OER activity of the nanocomposites. LSV polarization curves using (a) 0.1 M NaP_i buffer with 1 M $NaNO_3$ as an electrolyte at pH 6.9 and (b) 1 M KOH electrolyte at pH 14.2. (c) Extracted Tafel slopes. (d) Estimated ECSA values.

conditions, Co_9/Mg_2Al shows an onset overpotential of 530 mV and a Tafel slope of 73 mV dec^{-1} (Fig. 3(c) and Fig. S14), indicating a competition between a chemical and an electron-transfer limiting step. Co_4-WD/Mg_2Al displays an onset overpotential of 595 mV and a Tafel slope of 205 mV dec^{-1}. The rather large Tafel slope indicates that the OER is limited by a diffusion process and electron transfer. The latter values are comparable to those obtained for Co_4/Mg_2Al, which shows an onset overpotential of 600 mV and a Tafel slope of 195 mV dec^{-1}. Our results indicate that Co_9 possesses superior OER kinetics and that, when carefully engineered to overcome the steric hindrance of bulky POM ligands, Co_4-WD-based nanocomposites can display comparable OER capabilities to Co_4-based ones. This is reasonable since both Co-POMs share the same OER-active cobalt-oxo belt in the sandwich structure.

The abovementioned *ex situ* characterisation showed that Co-POMs decompose under alkaline conditions, leading to the *in situ* formation of layered CoO_x. Indeed, we observe the appearance of a new redox pair in the pre-conditioning CVs, which can be assigned to the $Co^{2+/3+}$ redox pair of CoO_x (Fig. S15). We conducted LSV measurements at pH 14.2 to study the differences in the catalytic activity of the CoO_x formed by each Co-POM. The normalised polarization curves in Fig. 3(b) show that the three materials display similar OER activities but with some differences worth mentioning. The Co_9/Mg_2Al-derived hybrid shows a higher intrinsic OER activity with an onset overpotential of 320 mV. Notably, despite sharing the same catalytic site, the Co_4-WD/Mg_2Al-derived material shows lower OER capabilities than that of the Co_4/Mg_2Al-derived material, with onset overpotentials of 350 mV and 335 mV, respectively. Additionally, they all follow the same Tafel behaviour with Tafel slopes close to 40 mV/dec, as shown in Fig. 3(c) and Fig. S14, which is reasonable given the similarity of the formed oxides and indicates a rate-limiting step

corresponding to the second-electron oxidation, *i.e.*, the formation of the Co–O species. The observed behaviour suggests that the POM ligand may influence the structure of the formed CoO_x and, therefore, the overall OER properties. In fact, the calculated ECSA values for these Co-POM/Mg_2Al-derived materials demonstrate a distinct number of active sites in the formed CoO_x (Fig. 3(d)).

Chronoamperometric measurements were performed to assess the long-term stability of the nanocomposites under OER conditions (Fig. S16). In this case, we used carbon paper as working electrodes, enabling *in situ* XPS characterization after 24 hours of water electrolysis. Fig. S17 and S18 show the high-resolution XPS spectra of the hybrids after catalysis at pH 6.9 and pH 14.2 compared with those of the fresh materials. Although Co_4-WD and Co_9 are generally stable near neutral pH and prone to hydrolysis in strongly alkaline media, it remained unclear whether this behaviour persisted during electrocatalysis. In all postcatalytic samples, the Mg and Al signals of the LDH are preserved, indicating that the layered host structure remains intact regardless of the pH. In contrast, the W 4f and Co 2p regions show pronounced differences depending on the operating conditions. At pH 6.9, the W : Co ratios of the hybrids ($Co_9/Mg_2Al \approx 2.8$; Co_4-WD/$Mg_2Al \approx 2.7$) remain close to those of the fresh materials ($Co_9/Mg_2Al \approx 2$; Co_4-WD/$Mg_2Al \approx 4$), demonstrating that the POM frameworks are retained in the interlayer space after OER operation. Note that these ratios are lower than expected since XPS is a surface technique, thus precluding the exact quantification of intercalated POMs. At pH 14, however, the W : Co ratio drops drastically (~ 0.05 for both hybrids), evidencing the loss of W-containing fragments and therefore decomposition of the POM clusters. The remaining cobalt persists within the LDH interlamellar space. Concomitantly, the Co 2p spectra show attenuation of the characteristic Co(II) satellite features, indicating partial oxidation to a mixed Co(II)/Co(III) state, an effect absent in the samples operated at pH 6.9. TEM images and EDX mapping of the recovered samples also agree with those observations (Fig. S19–S22). FT-IR spectra show the expected bands associated with the POMs at pH 6.9 and a decrease of these at pH 14.2 (Fig. S23). Together, these results demonstrate that intercalation within the LDH stabilizes both Co_4-WD and Co_9 POMs under OER conditions at neutral pH, preserving their composition and oxidation state. In strongly alkaline media, however, the clusters rapidly decompose, leaving only oxidized cobalt species confined in the LDH layers.

In conclusion, we have prepared different Co-POM/Mg_2Al nanocomposites and studied their OER properties. At pH 6.9, the Co_9/Mg_2Al hybrid displays superior intrinsic activity. Interestingly, confinement effects activate the Co_4-WD POM, as seen from the comparable activity displayed by Co_4-WD/Mg_2Al and Co_4/Mg_2Al. Conversely, at pH 14.2, the LDH environment cannot stabilise the POM framework, leading to POM decomposition and *in situ* formation of OER active layered CoO_x species in the LDH gallery space. The latter can be exploited as a unique method for the controlled synthesis of layered metal oxides. Moreover, the properties of the formed layered CoO_x can be fine-tuned by carefully selecting the Co-POM with the appropriate nuclearity.

Javier Quirós-Huerta: investigation. Ramón Torres-Cavanillas: data curation, formal analysis (XPS analysis), and writing – review and editing. Susana Ochando-Pariente: investigation. Eugenio Coronado: validation and writing – review and editing. Joaquín Soriano-López: conceptualisation, supervision, investigation, data curation, formal analysis, and writing – original draft.

Conflicts of interest

There are no conflicts to declare.

Data availability

Data for this article are available at the Zenodo repository DOI: https://doi.org/10.5281/zenodo.18772842 and will be made available after acceptance.

Supplementary information (SI): instrumentation and methodology, materials and synthetic details, electrochemical procedures, and characterisation of the materials. See DOI: https://doi.org/10.1039/d6cc01200k.

Acknowledgements

This work was supported by the EU (ERC Proof of Concept Grant 2D4H2 No. 101101079 and Pathfinder-4D-NMR 101099676), the Spanish MCIN (PID2022-143297NB-I00, PID2020-117152RB-I00, and TED2021-131347B-I00), the Generalitat Valenciana (PROMETEO Program CIPROM/2024/51), and the Unit of Excellence "Maria de Maeztu" CEX2019-000919-M. J. S.-L. acknowledges the funding from Generalitat Valenciana through the Plan Gen-T of Excellence (CDEIGENT/2021/037). R. T.-C. thanks the University of Valencia for the Banco Santander grant (Santander UV25-23). This study forms part of the Advanced Materials program (MFA/2022/050) and was supported by MCIU with funding from the European Union NextGenerationEU (PRTR-C17.I1) and by Generalitat Valenciana.

References

1 L. Chen, G. Msigwa, M. Yang, A. I. Osman, S. Fawzy, D. W. Rooney and P.-S. Yap, *Environ. Chem. Lett.*, 2022, **20**, 2277–2310.
2 I. Staffell, D. Scamman, A. Velazquez Abad, P. Balcombe, P. E. Dodds, P. Ekins, N. Shah and K. R. Ward, *Energy Environ. Sci.*, 2019, **12**, 463–491.
3 S. Singh, S. Jain, P. S. Venkateswaran, A. K. Tiwari, M. R. Nouni, J. K. Pandey and S. Goel, *Renewable Sustainable Energy Rev.*, 2015, **51**, 623–633.
4 N. Wen, X. Jiao, Y. Xia and D. Chen, *Mater. Chem. Front.*, 2023, **7**, 4833–4864.
5 M. J. Craig, G. Coulter, E. Dolan, J. Soriano-López, E. Mates-Torres, W. Schmitt and M. García-Melchor, *Nat. Commun.*, 2019, **10**, 4993.
6 Z. Feng, C. Dai, P. Shi, X. Lei, R. Guo, B. Wang, X. Liu and J. You, *Chem. Eng. J.*, 2024, **485**, 149992.
7 E. Fabbri and T. J. Schmidt, *ACS Catal.*, 2018, **8**, 9765–9774.
8 I. Roger, M. A. Shipman and M. D. Symes, *Nat. Rev. Chem.*, 2017, **1**, 0003.
9 J. Yu, S. Giancola, B. Khezri, D. Nieto-Castro, J. Redondo, F. Schiller, S. Barja, M. C. Spadaro, J. Arbiol, F. A. Garcés-Pineda and J. R. Galán-Mascarós, *EES Catal.*, 2023, **1**, 765–773.
10 B. Fabre, C. Falaise and E. Cadot, *ACS Catal.*, 2022, **12**, 12055–12091.

11 Q. Hu, H. Zhou, Y. Ding, T. Wågberg and X. Han, *ACS Catal.*, 2024, **14**, 5898–5910.
12 Q. Yin, J. M. Tan, C. Besson, Y. V. Geletii, D. G. Musaev, A. E. Kuznetsov, Z. Luo, K. I. Hardcastle and C. L. Hill, *Science*, 2010, **328**, 342–345.
13 M. Blasco-Ahicart, J. Soriano-López, J. J. Carbó, J. M. Poblet and J. R. Galan-Mascaros, *Nat. Chem.*, 2018, **10**, 24–30.
14 X.-B. Han, Z.-M. Zhang, T. Zhang, Y.-G. Li, W. Lin, W. You, Z.-M. Su and E.-B. Wang, *J. Am. Chem. Soc.*, 2014, **136**, 5359–5366.
15 K. Azmani, M. Besora, J. Soriano-López, M. Landolsi, A.-L. Teillout, P. de Oliveira, I.-M. Mbomekallé, J. M. Poblet and J.-R. Galán-Mascarós, *Chem. Sci.*, 2021, **12**, 8755–8766.
16 J. Soriano-López, F. W. Steuber, M. Mulahmetović, M. Besora, J. M. Clemente-Juan, M. O'Doherty, N.-Y. Zhu, C. L. Hill, E. Coronado, J. M. Poblet and W. Schmitt, *Chem. Sci.*, 2023, **14**, 13722–13733.
17 M. Martin-Sabi, J. Soriano-López, R. S. Winter, J.-J. Chen, L. Vilà-Nadal, D.-L. Long, J. R. Galán-Mascarós and L. Cronin, *Nat. Catal.*, 2018, **1**, 208–213.
18 H. Lv, J. Song, Y. V. Geletii, J. W. Vickers, J. M. Sumliner, D. G. Musaev, P. Kögerler, P. F. Zhuk, J. Bacsa, G. Zhu and C. L. Hill, *J. Am. Chem. Soc.*, 2014, **136**, 9268–9271.
19 M. Tao, Q. Yin, A. L. Kaledin, N. Uhlikova, X. Lu, T. Cheng, Y.-S. Chen, T. Lian, Y. V. Geletii, D. G. Musaev, J. Bacsa and C. L. Hill, *Inorg. Chem.*, 2022, **61**, 6252–6262.
20 T. Ahmed, M. A. Asghar, A. Ali, Z. Akhter, S. Ali, I. Ullah, T. Nisar, V. Wagner, S. Touseef, A. Hussain and A. Haider, *J. Alloys Compd.*, 2022, **909**, 164709.
21 W. A. Shah, X. Dai, X. Zhai, Y. Zhao, Y. Zhang and S. Li, *Commun. Chem.*, 2025, **9**, 29.
22 R. Gong, D. Mitoraj, D. Gao, M. Mundszinger, D. Sorsche, U. Kaiser, C. Streb, R. Beranek and S. Rau, *Adv. Sustainable Syst.*, 2022, **6**, 202100473.
23 I. Brotons-Alcázar, R. Torres-Cavanillas, M. Morant-Giner, M. Cvikl, S. Mañas-Valero, A. Forment-Aliaga and E. Coronado, *Dalton Trans.*, 2021, **50**, 16281–16289.
24 R. Torres-Cavanillas and A. Forment-Aliaga, *Commun. Chem.*, 2024, **7**, 241.
25 J. Soriano-López, J. Quirós-Huerta, Á. Seijas-Da Silva, R. Torres-Cavanillas, E. Andres-Garcia, G. Abellán and E. Coronado, *Inorg. Chem.*, 2025, **64**, 3242–3255.
26 S. P. Newman and W. Jones, *New J. Chem.*, 1998, **22**, 105–115.
27 D. S. Charles, M. Feygenson, K. Page, J. Neuefeind, W. Xu and X. Teng, *Nat. Commun.*, 2017, **8**, 15520.
28 N. I. Gumerova and A. Rompel, *Chem. Soc. Rev.*, 2020, **49**, 7568–7601.
29 D. Lieb, A. Zahl, E. F. Wilson, C. Streb, L. C. Nye, K. Meyer and I. Ivanović-Burmazović, *Inorg. Chem.*, 2011, **50**, 9053–9058.
30 S. Goberna-Ferrón, J. Soriano-López, J. R. Galán-Mascarós and M. Nyman, *Eur. J. Inorg. Chem.*, 2015, 2833–2840.
31 S. Goberna-Ferrón, L. Vigara, J. Soriano-López and J. R. Galán-Mascarós, *Inorg. Chem.*, 2012, **51**, 11707–11715.
32 J. T. Arens, M. Blasco-Ahicart, K. Azmani, J. Soriano-López, A. García-Eguizábal, J. M. Poblet and J. R. Galán-Mascaros, *J. Catal.*, 2020, **389**, 345–351.